Geophysical Journal International

Geophys. J. Int. (2011) **184,** 287–300 doi: 10.1111/j.1365-246X.2010.04830.x

Directionality analysis and Rayleigh wave tomography of ambient seismic noise in southern Norway

Andreas Köhler, Christian Weidle and Valérie Maupin

Department of Geosciences, University of Oslo, Post Box 1047, 0316 *Oslo, Norway. E-mail: andreas.kohler@geo.uio.no*

Accepted 2010 September 27. Received 2010 September 22; in original form 2010 May 12

SUMMARY

We process seismic broad-band data from southern Norway by cross correlation of ambient seismic noise in view of getting a better image of the crustal structure in the area. The main data set sterns from the temporary MAGNUS network which operated continuously from 2006 September to 2008 June. Additionally, data from permanent stations of the National Norwegian Seismic Network, the NORSAR array and GSN stations in the region are used. We compute vertical component cross-correlation functions using 41 receivers for 3-month time windows. Evaluation of the azimuthal and temporal variation of signal-to-noise ratios (SNRs) and f–k analysis of data from NORSAR array between 3 and 25 s period shows that the dominant source areas of seismic noise are located to the west and north of the network during most of the measurement time, which corresponds well to the Norwegian coast line. During summer months, the SNRs decrease but the azimuthal distribution becomes more uniform between 7 and 12 s period, suggesting a more diffuse character of the wavefield. Primary ocean microseisms above 12 s show different dominant source azimuths during this time period compared to the winter months. Time–frequency analysis is applied to measure Rayleigh wave group velocity dispersion curves between each station pair for each 3-month correlation stack and the mean and variance of all dispersion curves is computed for each path. After rejection of low-quality data, a careful analysis shows that the group velocities are not biased by noise directionality. We invert the data for group velocity maps at period bands between 3 and 25 s. At short periods, we find an average Rayleigh wave group speed of about 3 km s^{-1} and velocity anomalies that correlate very well with local surface geology. While higher velocities (+5 per cent) can be associated with the Caledonian nappes in the central part of southern Norway, the Oslo Graben is reflected by negative velocity anomalies (−3 to −5 per cent). At longer periods, group velocities correlate well with the variation of Moho depths beneath southern Norway.

Key words: Interferometry; Surface waves and free oscillations; Seismic tomography; Crustal structure; Europe.

1 INTRODUCTION

The use of ambient seismic noise to infer the Earth's structure is becoming an increasingly popular and established approach. Due to its permanent availability and the main energy contribution at comparatively short periods, seismic noise has the capability to fill the gap in conventional seismological data which exists due to lack of earthquakes on local and regional scales. Aki (1957) suggested an autocorrelation method which allows to estimate phase velocities of surface waves based on the stochastic character of the noise wavefield. Also in other disciplines, like acoustics (Roux & Kuperman 2004) and helio-seismology (Duvall *et al.* 1993), the potential to infer velocity information or coherent wave fronts from a diffuse wavefield has been recognized (see also Larose *et al.* 2006). In seismology, Shapiro & Campillo (2004) and Sabra *et al.* (2005a) have been among the first authors who showed that cross correlation of noise seismograms reveals the surface wave Green's function between two receivers, and can be used to invert for group velocity maps (Sabra *et al.* 2005b; Shapiro *et al.* 2005). Rayleigh wave tomographies based on seismic noise have since been published for various regions in recent years and have confirmed the reliability of this approach in practice (e.g. Gerstoft *et al.* 2006; Yang *et al.* 2006; Moschetti *et al.* 2007; Lin *et al.* 2007; Stehly *et al.* 2009). Moreover, the use of phase velocities and Love waves for ambient noise tomographies has been demonstrated (Lin *et al.* 2008; Yao *et al.* 2006, 2008).

Theoretical derivations have confirmed the observation of empirical Green's functions by cross correlation but also revealed the limitations of that method (Snieder 2004; Roux *et al.* 2005; Gouédard *et al.* 2008). In particular, the requirement of noise sources uniformly distributed over azimuth has been pointed out. Recently, several authors studied and quantified the effect of non-isotropic noise distribution on the Green's function estimate (Tsai 2009; Weaver *et al.* 2009; Yao & van der Hilst 2009). Tsai (2009) quantified the errors due to non-uniform medium between receivers and anisotropic source distribution in a ray-theoretical framework. The study showed that velocity estimates can vary significantly when assumptions are not fulfilled (2–3 per cent deviation in velocity). Weaver *et al.* (2009) found that the effect is small, provided that a sufficiently smooth non-isotropic source distribution exists. Therefore, careful quality assessment and test of the directionality of noise is mandatory to achieve reliable tomographical models. Within this context, Bensen *et al.* (2007) gave practical recommendations for the processing of seismic noise and selection of suitable Green's function estimates. Furthermore, seasonal variation of the seismic noise wavefield and its impact on cross-correlation functions have been studied (Stehly *et al.* 2006; Pedersen *et al.* 2007; Stehly *et al.* 2008).

It has been discovered very early in the history of seismology that the main origin of seismic noise is the ocean swell on coasts (Gutenberg 1936). Direct interaction between ocean gravity waves and sea bottom generates primary microseisms between 12 and 25 s period. Furthermore, secondary microseisms are observed between 3 and 10 s period. Secondary microseisms are interpreted as generated by interfering water waves travelling in opposite directions towards and away from the coast in localized regions close to the shoreline (Longuet-Higgins 1950; Friedrich *et al.* 1998). For primary microseisms, different explanations and observations have been published. While Friedrich *et al.* (1998) described and observed the origin close to the shorelines, Stehly *et al.* (2006) identified source areas within the deep ocean and suggested, therefore, an origin different from secondary microseisms. Amplitudes of seismic noise can be correlated with activity of low pressure areas or wave heights in the oceans (Essen *et al.* 2003; Stehly *et al.* 2006). Furthermore, Stehly *et al.* (2006) found that the source directions corresponding to the secondary microseismic peak are more stable compared to primary microseisms.

In this study, we compute noise cross-correlation functions (NCFs) from seismic noise recorded on a temporary seismic network in southern Norway. The present crustal and shallow uppermantle structure beneath southern Norway is, contrary to the offshore areas, poorly mapped. However, a good understanding of the geometry and parameters of the crust is relevant to understand the uplift history of the Scandes mountain range in the western part of the Fennoscandian shield (Weidle *et al.* 2010). Recently, a new regional surface wave tomography model for northern Europe (Weidle & Maupin 2008) and constraints for Moho depths along three seismic profiles through southern Norway (Stratford *et al.* 2009) gave more insights into the regional structure. However, more information on a smaller scale, in particular a 3-D model for the lithosphere, is still required to constrain geodynamic models. Using data from the MAGNUS seismic network in southern Norway (Weidle *et al.* 2010), cross correlation of ambient noise is a first step towards such a model for the crust and shallow uppermantle structure. In this study we give a detailed quality assessment of the applied procedure, and present results from Rayleigh wave group velocity tomography in the period range 3–25 s in the studied region.

2 DATA PREPARATION

2.1 Processing

We employ 20 months of data from the 41 seismic broad-band receivers of the MAGNUS network (Fig. 1). In addition to permanent stations (NORSAR array, BER, KONO, HFC2), the network included a temporary installation of 23 STS-2, six KS2000 and two CMG-40T instruments, which recorded continuously with a sampling rate of 50 Hz. All stations were acquiring data between 2006 September and 2008 June. We process data following the recommendations of Bensen *et al.* (2007). After correction for instrument response, offset removal, bandpass filtering between 0.5 and 100 s period and downsampling to 10 Hz, we compute the NCF for each station pair using the vertical seismogram component of 15-min-long time windows. Prior to that, time domain normalization is required to suppress the effect of strong directional sources like earthquakes. We find that weighting down high amplitudes by a running absolute mean as suggested by Bensen *et al.* (2007) produces the most reliable NCFs. In addition, we pre-whitened the spectrum in the frequency domain to remove biases related to the strong second microseismic peak. After spectral normalization, the spectrum is again tapered between 0.5 and 100 s period and the cross spectrum is built. The emergence of signals in the cross-correlation function is depending on the considered wavelength, the interstation distance and the duration of correlation. Given the absence of strongly directional noise or considering only well-oriented station pairs, Bensen *et al.* (2007) showed that individual NCF stacks over 3 months produce reliable Green's function estimates (SNR above 10) for period bands shorter than 25 s using GSN stations within the United States. The authors suggested to use those stacks to assess the measurement uncertainty. Therefore, we transform the 15-min cross spectrum back into time domain and stack it over time intervals of 3 months duration with 1 month overlap. Furthermore, a stack over 20 months (2006 November–2008 June) is prepared for each station pair. We determine group velocity dispersion curves in a period range from 0.5 to 100 s for all 18 3-month stacks and the 20-month stack by applying time frequency analysis (FTAN, Levshin *et al.* 1989; Ritzwoller & Levshin 1998). Subsequently, an averaged dispersion curve and its standard deviation is estimated from the measurements on the different 3-month stacks.

2.2 Quality assessment and data selection

2.2.1 SNR and f–k analysis

Fig. 2 shows a selection of NCFs for two different azimuthal ranges of station pair orientation (20-month stack). Clear causal (energy travelling from western to eastern half-plane) and acausal signals can be observed. The moveout of about 3 km s^{-1} corresponds well to crustal surface wave velocities. However, the amplitudes and period content of signals differ clearly between positive and negative sides. Station pairs oriented southwest–northeast (Fig. 2a) show comparable amplitudes on both sides, but shorter periods are observed for the causal signal. On the other hand, causal signals show clearly higher amplitudes than acausal parts perpendicular to that direction (Fig. 2b). The observations of asymmetric NCFs reveal a dominant noise propagation direction from northwest towards southeast. However, the presence of clear acausal signals is evidence for a wider azimuthal distribution of sources. The difference in the frequency content may exist due to the varying energy contribution of primary and secondary ocean microseisms over azimuth.

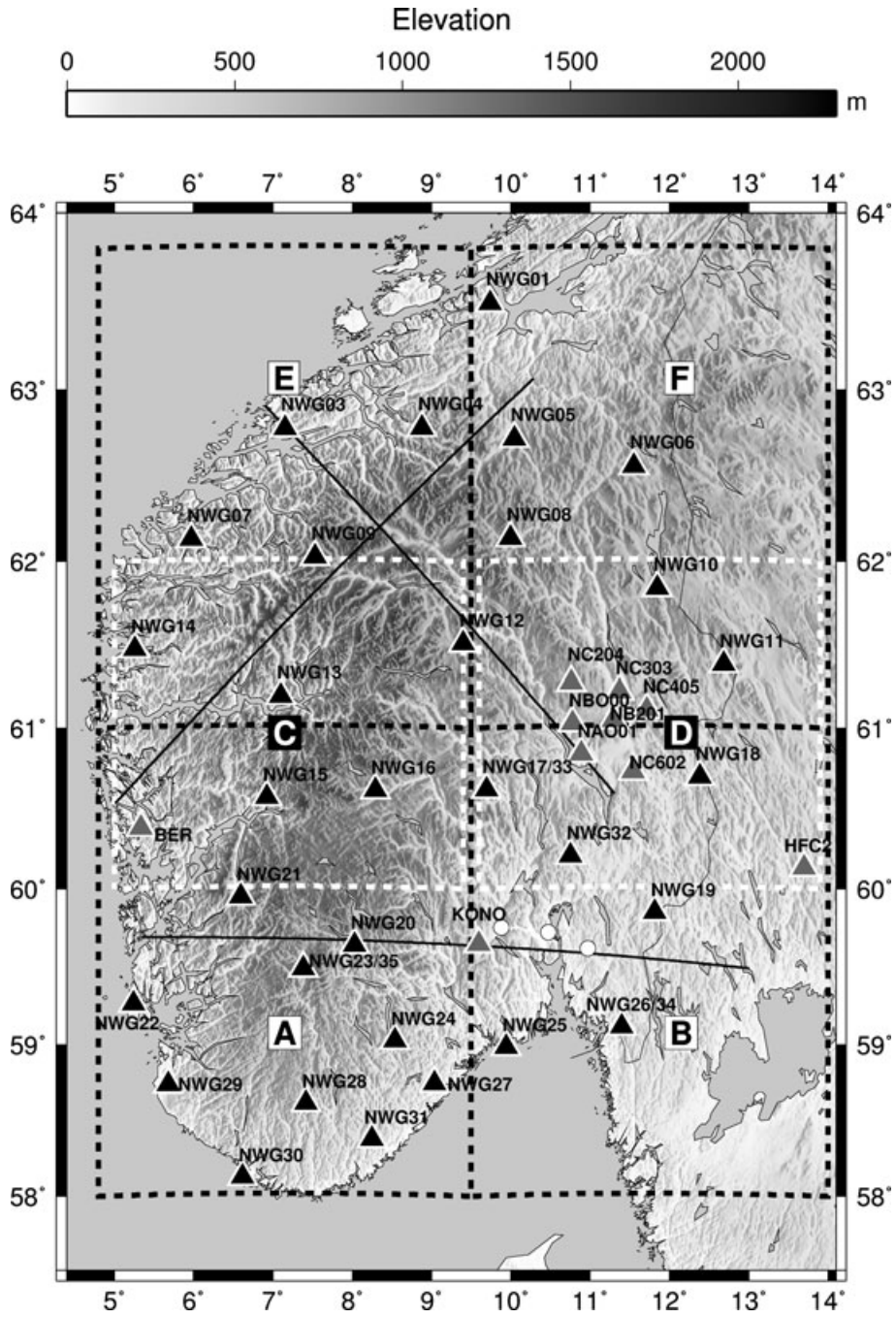

Figure 1. MAGNUS seismic network in southern Norway. Black triangles indicate temporary and grey permanent broad-band stations. Dashed lines confine overlapping subnetworks A to F which are used to analyse the seismic noise directionality in Fig. 4. Straight black lines show approximate location of the three lines of the MAGNUS-REX experiment (Stratford *et al.* 2009). White-filled circles indicate locations where results are compared quantitatively with our noise tomography.

For a more detailed and quantitative test of noise directionality, the SNR of a NCF can be used as an estimate for the source azimuth distribution (Gerstoft *et al.* 2006). We compute SNRs in decibels for all station pairs separately for the causal and acausal signals. As signal amplitude, we take the maximum envelope in a time windows between $t_{\min} = d/3.3\,\mathrm{km\,s^{-1}} - \tau_{\max}$ and $t_{\max} = d/2.6\,\mathrm{km\,s^{-1}} + 2 \cdot \tau_{\max}$, where $\tau_{\max}$ is the maximum period of the bandpass filter and d the interstation distance (Bensen *et al.* 2007). The noise amplitude of the NCF trace is computed as the rms of the envelope between 500 and 1500 s. For example, for those two NCFs corresponding to the smallest interstation distances in Fig. 2, we obtain broad-band SNRs for acausal/causal sides of about 27/33 (Fig. 2a) and 27/32 (Fig. 2b), respectively. For period-dependent SNRs, we apply bandpass filters directly on the NCFs.

It has been shown theoretically and in laboratory experiments that there is a square root dependence between stack length and SNR for a homogeneous distribution of noise sources (Larose *et al.* 2007). This behaviour has been confirmed in practice by Sabra *et al.* (2005a) and Gerstoft *et al.* (2006) for maximum stacking intervals of about 1 month. However, Bensen *et al.* (2007) showed that the

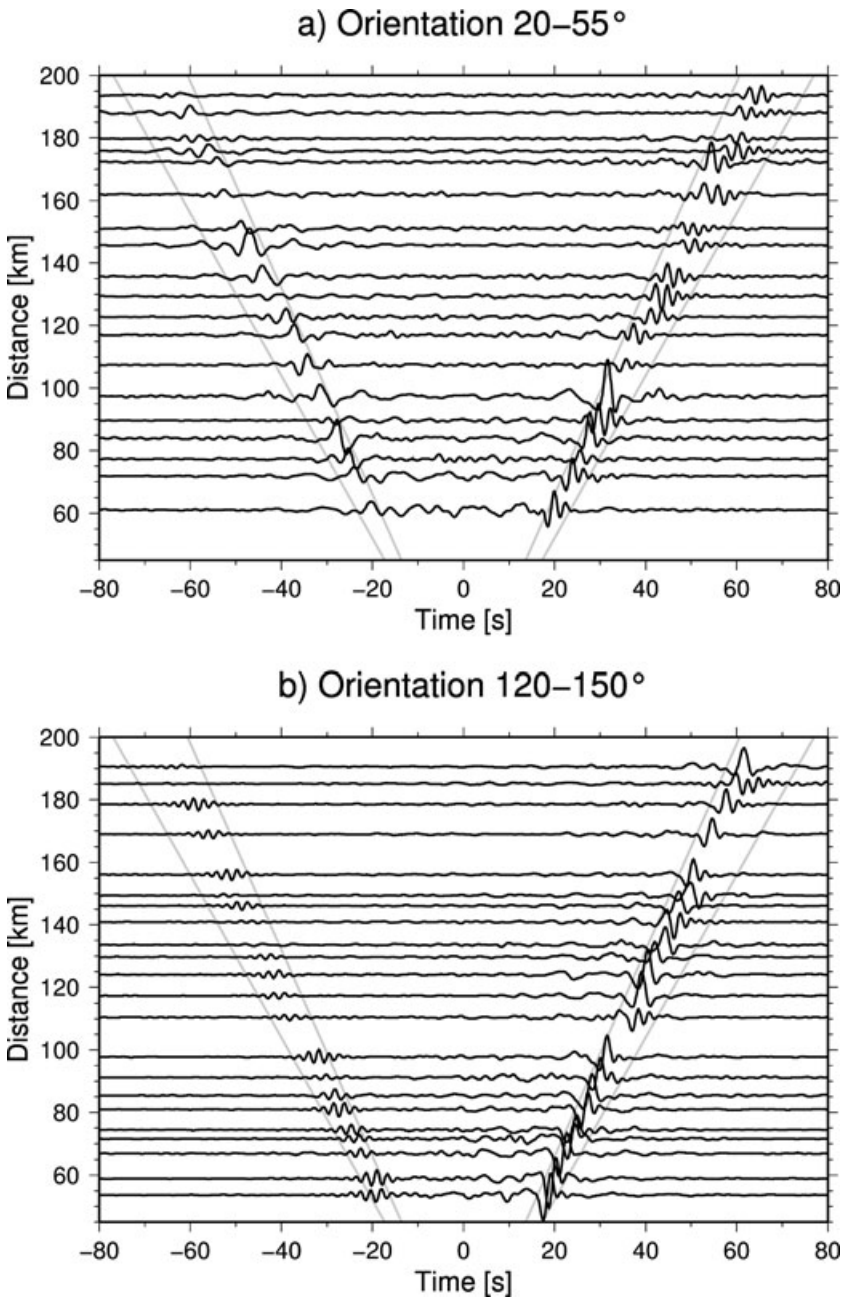

Figure 2. Selected noise cross-correlation functions filtered between 2 and 12.5 s period for two different ranges of orientation. Grey lines indicate traveltimes corresponding to velocities of 2.6 and 3.3 km s^{-1}. Causal (positive) signals correspond to energy travelling from western to eastern half-plane. Azimuth is measured clockwise from North.

emergence rate of empirical Green's function need not to correspond necessarily to a power law with an exponent of 0.5 for longer stacks. Depending on the period and station pair, lower exponents have been observed. Fig. 3(a) confirms the power-law dependence between SNRs and stack length for our data. We also do not observe a square root dependence, probably due to the anisotropic distribution of noise sources. Figs 3(b) and (c) show the distribution of SNRs of all station pairs for three period bands and both the 20-month and the 3-month stacks. The maximum in the SNR distribution for the 20-month stack is located above SNR = 20 at 3 and 12 s period, what might be an effect of the primary and secondary microseismic peaks. At 7 s, more station pairs have SNRs lower than 20, which can be explained by lack of energy for period bands in-between the microseismic peaks. The SNR distributions are slightly shifted towards higher values compared to the 3-month stack.

Fig. 4 shows the variation of broad-band SNRs over time (3-month stacks) and as a function of receiver azimuth for six overlapping subnetworks (see Fig. 1). The highest SNRs are observed for station pairs with azimuths between −135° (southwest) and 45° (northeast). Therefore, the major generation areas of seismic noise would be located in general to the west and north of the network. This is not surprising given the geography of the Norwegian coastlines. We observe decreasing SNRs in that dominant azimuthal range during summer months. This seasonal variation is more pronounced for seismic noise coming from northwest to north, whereas the western direction remains much more stable. Slightly different SNR

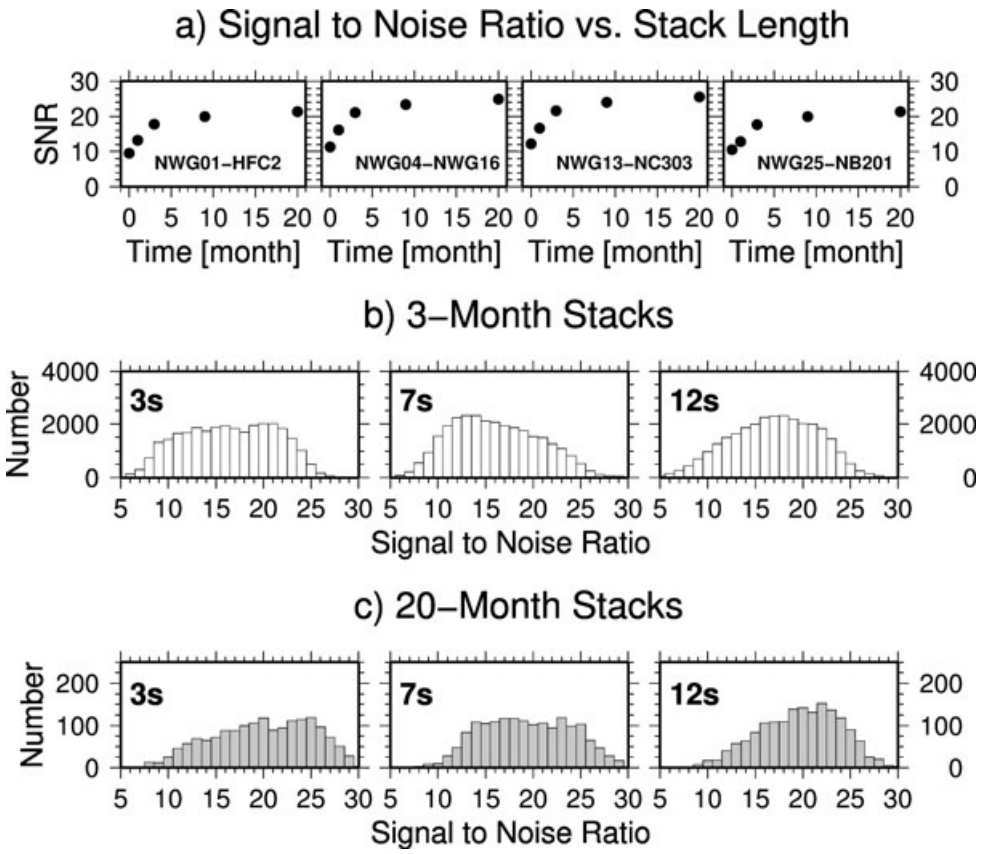

Figure 3. Statistics on signal-to-noise ratios (SNRs) of cross-correlation functions. (a) SNRs for four different station pairs are plotted versus stack length (1 d, 1 month, 3 months, 9 months, 20 months). (b) Histograms of SNRs for three period bands. Numbers of cross-correlation functions having a given SNR are computed from 3-month time intervals. (c) Numbers of cross-correlation functions obtained from entire record (20 months) are presented.

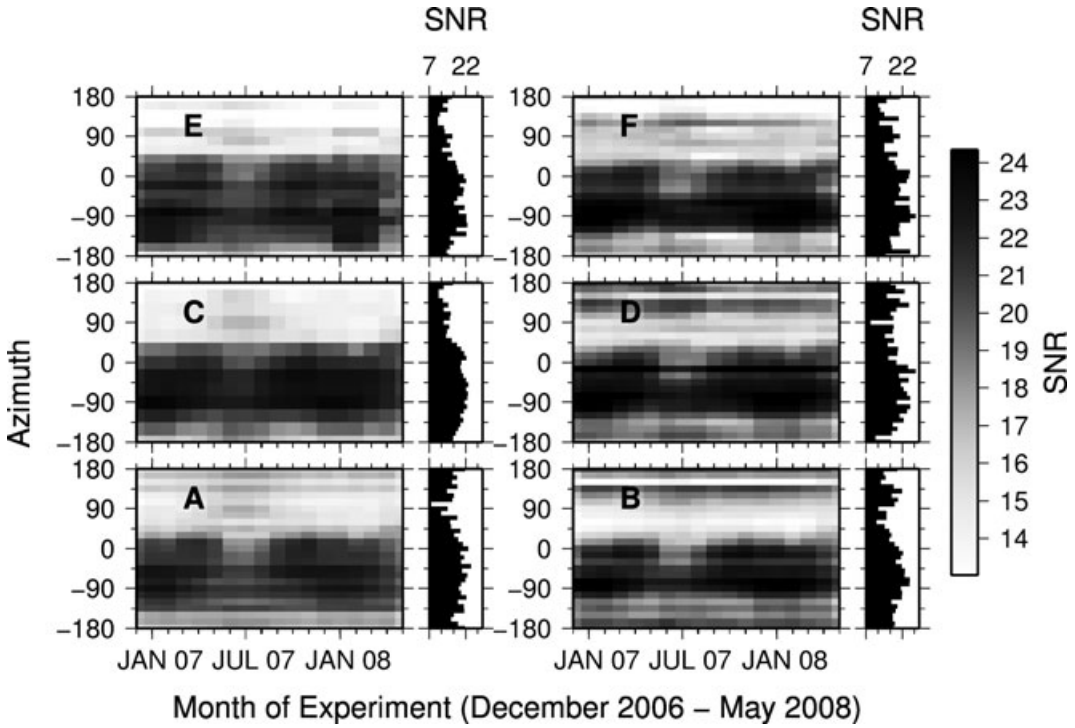

Figure 4. Temporal and spatial variation of signal-to-noise ratios (SNRs) computed from noise cross-correlation functions stacked over 3 months. Panels A–F show broad-band SNRs for six station groups (see Fig. 1). Small panels show SNRs averaged over time for each station group. Azimuth is measured clockwise from North.

distributions are obtained for the six subnetworks, which reflects the proximity of receivers with respect to the coastlines (Fig. 1). For station groups B, D and F, which are located to the east, the azimuthal range with the highest SNRs is slightly narrower compared to A, C and E, which are located along the coast. This can be explained by the fact that the eastern stations see the noise generating areas in a smaller azimuth range. This would indicate that the dominant noise source areas for southern Norway are local coasts, rather than other known and more distant source regions like northern Norway (Friedrich *et al.* 1998). For the eastern subnetworks B, D and F, we observe the existence of a narrow source direction (to the south and southeast), which are too weak to be seen in the West. An explanation for the southern source as seen from B and D, could be seismic noise generated within the Oslo Fjord region.

In Fig. 5(a) we show the azimuthal variation of SNRs for six different period bands containing primary and secondary microseisms. Furthermore, we present results of frequency–wavenumber (f–k) analysis of data from the NORSAR array (Fig. 5b) for the same period bands. Theoretically, the wavenumber limits given by the array characteristic imply that f–k analysis at 3 s period is critical. However, since results look still reasonable, we also show this period band. As an estimation for the semblance of a wavenumber vector $\vec{k}$, the following quantity is computed (Ohrnberger 2001):

$$S_{\vec{k}} = \frac{\sum_{f=f_{\rm low}}^{f_{\rm high}} \left| \sum_{m=1}^{M} Z_m(\omega_f) \exp(\mathrm{i}\omega_f \tau_m(\vec{k})) \right|^2}{M \sum_{f=f_{\rm low}}^{f_{\rm high}} \sum_{m=1}^{M} |Z_m(\omega_f)|^2}, \quad (1)$$

where $Z_m(\omega_f)$ is the discrete complex Fourier coefficient of the seismogram for station m (of M receivers in total) at the discrete angular frequency ω_f. The term $\tau_m(\vec{k})$ stands to traveltime delay. Variables $f_{\rm low}$ and $f_{\rm high}$ represent the indices of the lower and upper limit of the period band. f–k maps are computed for 15-min (pre-whitened) time windows and stacked over 1-month intervals. The maximum semblance values of all f–k maps are shown for each azimuth. The corresponding phase velocities vary between 3 and 4 km s^{-1}, which is consistent with the observed NCF moveout. Note that our

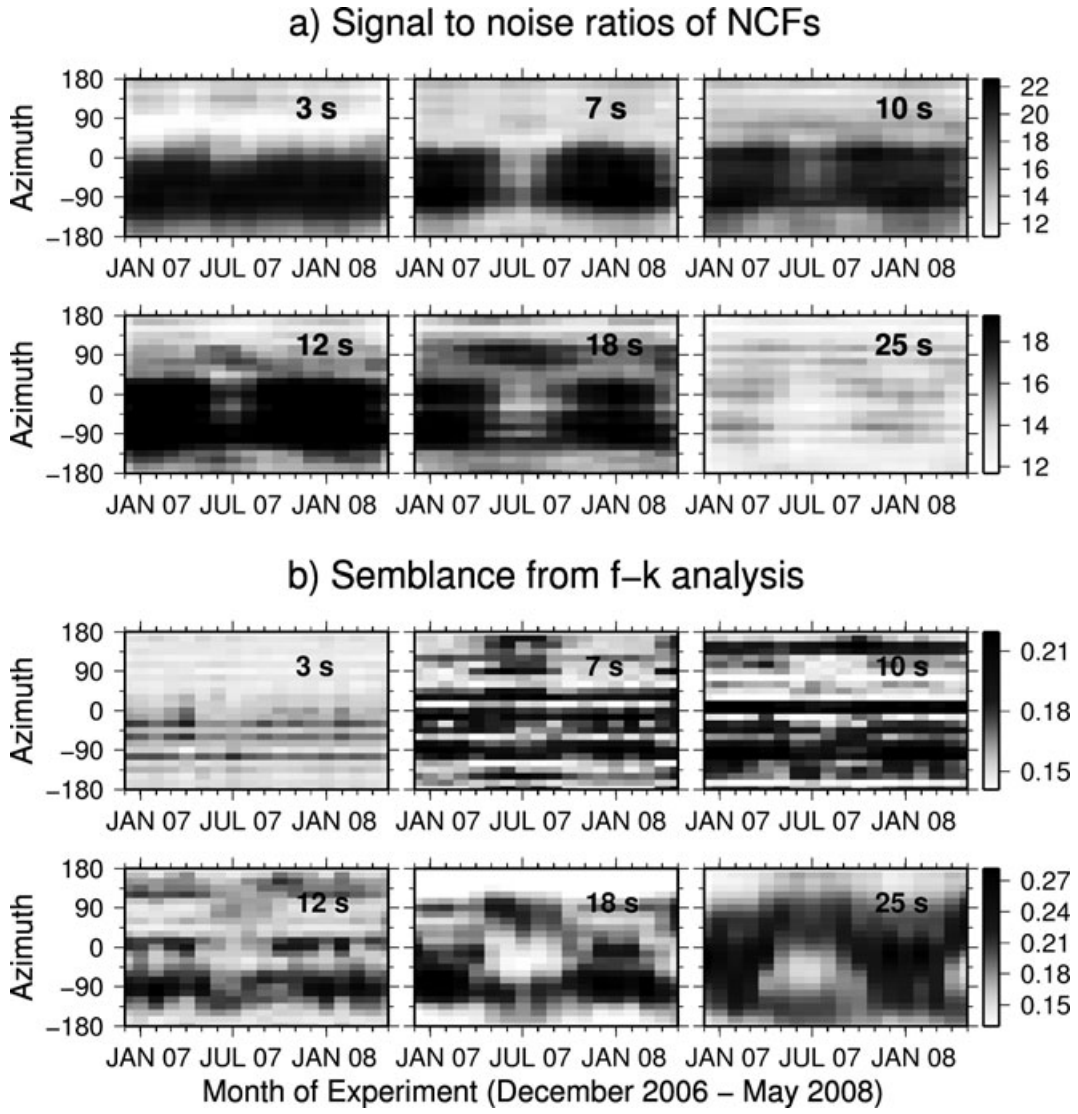

Figure 5. (a) Upper panels present SNRs of all NCFs for six period bands. (b) Lower panels show results of frequency–wavenumber (f–k) analysis using the NORSAR array for the same period bands. Temporal and azimuthal variation of semblance values is presented. Semblance values are obtained from f–k maps stacked over 1 month. The maximum semblance for each azimuth is shown (corresponding phase velocities lay around 3.5 km s^{-1}). Dark colours correspond to dominant directions in all panels (i.e. high semblance or high SNR).

semblance estimation is relative within each month, due to the spectral normalization, and semblance values cannot be compared between months. Therefore, Fig. 5(b) provides information about directionality of the wavefield at a given time interval, but does not reveal any noise energy variation during the year at a given azimuth, as Fig. 5(a) does.

Fig. 5 shows a good correspondence between large f–k semblance values and high SNRs considering the azimuthal as well as the temporal distribution. Looking at temporal changes in SNR and semblance as function of period for a particular azimuthal range, no clear seasonal variation can be observed at 3 s period. An explanation for the stability of secondary microseisms as seen at 3 s may be that the generation of seismic noise is less dependent on the seasonally varying storm activity. Within this period band, a low-amplitude, continuous ocean background swell seems to be sufficiently strong to excite the seismic noise wavefield in the studied area. Another explanation for temporal stable SNRs at 3 s could be that the noise is more randomized due to scattering at shorter periods. At longer periods, the character of seismic noise, that is, the azimuthal distribution, is clearly changing over the measurement period. SNRs and f–k azimuths reveal that seismic noise from secondary microseisms at 7 s period is more uniformly distributed in azimuth during summer. Also short-period primary microseisms (12 s) show a similar behaviour. This observation can be explained by less storm activity in the North Atlantic and therefore decreasing energy in oceanic microseisms generated at close shores. Nonetheless, primary microseisms are still dominant at azimuths between -45° and -90° during summer. The source areas of both kinds of microseisms seem to be similar during winter for all periods bands. In summer, however, the origin of long-period primary microseisms (longer than 12 s) as seen by SNRs and f–k semblance is dominantly northeast and southwest. Directions from west to north have a very low contribution. An explanation could be that primary and secondary microseisms are generated close to the coast in winter. Since nearby microseismic activity decreases during summer, more far noise sources are seen by the station network, that is, the deep ocean (Stehly *et al.* 2006) or distant shores. Similar to the SNRs of the eastern subnetworks (Fig. 4), f–k analysis reveals a narrow dominant source area southeast of the NORSAR array at 10 and 12 s period.

Our observations are in line with those of previous studies in that region. Friedrich *et al.* (1998) and Essen *et al.* (2003) analysed seismic noise for four and two winter months, respectively, using (among other networks) the NORSAR array. Friedrich *et al.* (1998) identified northern Norway and the British Isles as source zones between 12 and 18 s. Between 6 and 9 s the strongest source area was also found to be northern Norway. The authors suggested that secondary microseisms are continuously generated in discrete zones close to the coasts or within fjords. Essen *et al.* (2003) found that also the southwestern coast of Norway is a source region for secondary microseisms. They confirmed that seismic noise is controlled by wave heights within distinct generation areas. These regions are controlled by coastlines and bathymetry, rather than by the position of a storm itself. Pedersen *et al.* (2007) used NCFs and f–k analysis to discuss the character of seismic noise in northern Europe (i.e. plane wave versus diffuse wavefield). They analysed data recorded during winter on a broad-band network in Finland and on the NORSAR array. They found the noise wavefield to be strongly directional (close to plane wave) and not diffuse in Finland between 5 and 25 s (e.g. high semblance values for western direction). This introduced large, systematic errors in the group velocities obtained from NCFs for not optimally oriented station pairs. On the other hand, the authors showed that the noise between 1 and 4 s was coming from a wider range of azimuths (between south and east, clockwise), in agreement with our findings. However, our results suggest also reliable NCFs in Norway for periods longer than 5 s. Evidences for a more diffuse wavefield, like multiple source areas suggested by SNRs and f–k analysis, prevail compared to those for a pure plane wave character. In contrast to the setup in Pedersen *et al.* (2007), the noise source areas (i.e. the Norwegian coastlines) are better distributed around the receivers. Furthermore, we find the wavefield to be more diffuse during summer, a time interval which was not considered by the previous studies. We find also that the 3-month NCF stacks yield clear arrivals with acceptable SNRs. Therefore, it seems to be suitable to determine group velocity dispersion curve from each 3-month stack, separately. In doing so, we can estimate variations in group velocity measurements for different time periods and quantify the general uncertainty including changing noise directionality.

2.2.2 Group velocities

To assess potential inconsistencies between both arrivals, we decide to determine group velocities separately from the causal and acausal signals for each of the 18 3-month stacks, rather than using the symmetric component (Bensen *et al.* 2007). Hence, we can have a maximum of 36 independent velocity measurements for each station pair from which we compute mean and standard deviation. The individual group velocity dispersion curves are obtained interactively using the FTAN software (Levshin *et al.* 1989; Ritzwoller & Levshin 1998). In doing so, we manually select station pairs whose NCFs show a reasonable dispersive structure in a particular period range (i.e. a distinct and continuous dispersion branch within realistic velocity bounds). Fig. 6 shows the dispersion curves after averaging the velocity measurements from all 3-month stacks and both parts (causal and acausal if available) for four station pairs. We observe low standard deviations for period bands shorter than 15 s. Furthermore, independently of the orientation of station pair, the averaged velocities are in good agreement with the dispersion curves obtained directly from the 20-month stacks and from 3-month long stacks taken from summer and winter (causal and acausal if available). For period bands longer than 15 s, deviations between summer and winter can be observed, which are also reflected by increasing standard deviations determined from the 3-month stacks. Furthermore, Fig. 6 shows that the measured group velocities are reasonable since they vary around a reference Rayleigh wave group velocity dispersion curve. The reference dispersion curve is computed from a continental, crustal model with three layers over half-space [layer 1: interface depth 12 km, v_s gradient from 3.36 to 3.76 km s^{-1}; layer 2: interface depth 23 km, $v_s = 3.79$ km s^{-1}; layer 3: interface depth (Moho): 31 km, $v_s = 4.08$ km s^{-1}, halfspace: $v_s = 4.63$ km s^{-1}]. This model is routinely used to locate earthquakes with the Norwegian National Seismic Network (Havskov & Ottemöller 1999).

In addition to the manual pre-selection, we apply several data selection criteria to the NCFs and group velocity measurements to ensure a reliable data base for the tomography. First, each of the following criteria based on the SNRs of each station pair must be fulfilled:

(i) broad-band SNR higher than 12.5 for each 3-month NCF and each side of signal (causal and acausal);

(ii) broad-band SNR higher than 15 for 20-month NCFs;

(iii) SNR higher than 15 at each (filtered) target period for 20-month NCFs.

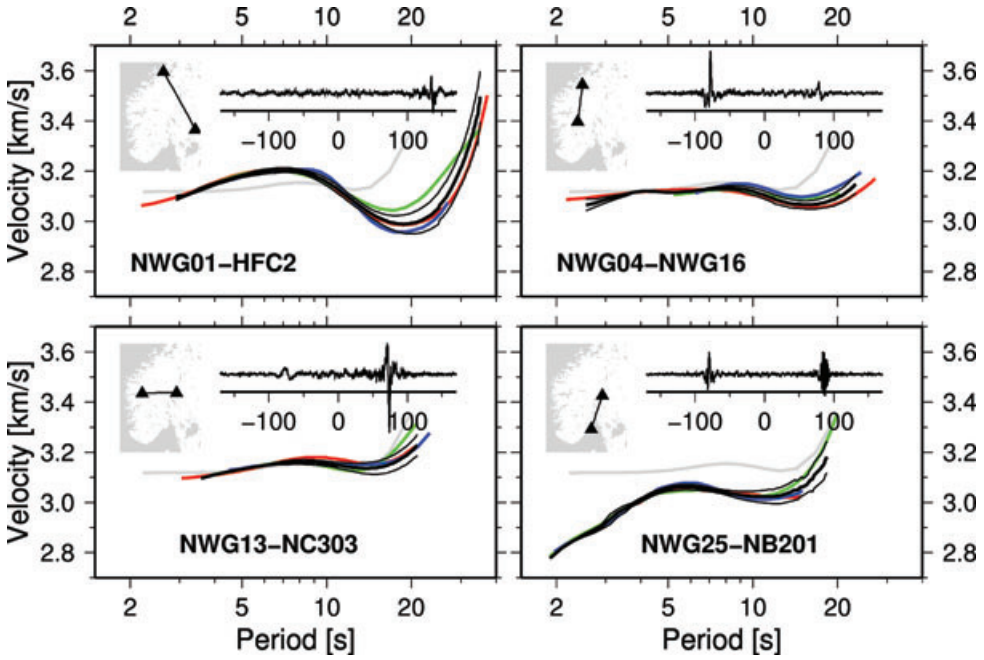

Figure 6. Rayleigh wave group velocity dispersion curves for four station pairs obtained by time–frequency analysis. Locations of receivers and corresponding noise cross-correlation functions (20-month stacks, scale is in seconds) are shown. Thick black line indicates dispersion curve averaged over all 3-month stacks. Thin lines show standard deviation. Coloured lines represent dispersion curve obtained from cross-correlation stacks over entire record (red), over summer months (green, June–August) and over winter months (blue, November–January), respectively. A dispersion curve is plotted in each panel (grey) which corresponds to a reference continental crust (see text).

Furthermore, the group velocity measurements obtained from all accepted NCFs must satisfy the following criteria at each period:

(i) number of velocity measurements from causal and acausal 3-month NCFs higher than three in total;
(ii) wavelength shorter than one-third of the interstation distance using an upper-bound estimate for the phase velocity of 4 km s^{-1} (see *f*–*k* analysis);
(iii) standard deviation of group velocity for all 3-month stacks lower than 0.05 km s^{-1};
(iv) 20-month group velocity within 1.5-times standard deviation of 3-month stacks.

Due to the geometry of the station network, more receiver pairs are available within an azimuthal range between −30° (150) and 75° (Fig. 7a). The selection process rejects comparable many of those measurements. An explanation could be too low SNRs for long interstation distances. Furthermore, since this range includes station pairs with azimuths around 45°, this could also be an effect of suboptimal orientations with respect to the dominant propagation direction of the noise.

Fig. 7(b) shows that the accepted group velocity measurements (those averaged over 3-month stacks) vary about 3–4 per cent around the mean of all station pairs at 3, 7 and 12 s period. This is only slightly higher than potential measurement uncertainties given by Tsai (2009). However, his findings are only valid for period bands longer than 10 s. Furthermore, Tsai (2009) showed that uncertainties increase with period within the valid range. At 12 s, the errors due to inhomogeneous medium between receivers and anisotropic source distribution have been found to be very low.

Fig. 7(b) shows also that the group velocities do not systematically depend on station pair orientation and interstation distance, as opposed to the observations by Pedersen *et al.* (2007) in Finland, where velocities are increasing significantly from 3 km s^{-1} to about 10 km s^{-1} for suboptimal orientations. For azimuths which could be considered as suboptimal in our study with respect to the dominant propagation direction of the noise (station pairs oriented southwest/northeast), no group velocity bias is observed in Fig. 7(b). Even though the noise distribution is not perfectly isotropic, we have neither strongly directional noise propagation nor are there azimuth ranges where noise is missing completely (see SNRs in Figs 4 and 5 at 3, 7 and 12 s period). In other words, the distribution is indeed non-isotropic, but also smooth. Following Weaver *et al.* (2009), the measurement error in velocity should therefore be small (see Section 1). Furthermore, the group velocity standard deviation of each station pair (estimated from 3-month stacks) reflects also the scatter introduced by annually changing noise directionality. In case there is a velocity bias to higher values during winter due to a strong and suboptimally oriented source, the more uniform source distribution in summer should yield a different and unbiased estimate. Since all velocity measurements are averaged, the standard deviation would increase. An inconsistency between causal and acausal velocity measurement will also increase the standard deviation due to the same reason. Thus, our pre-selection criterion ($\sigma_{\mathrm{vel}} < 0.05$ km s^{-1}) would reject those station pairs. Therefore, we have good indications that the distribution of noise sources, in combination with our data selection, is sufficient to avoid biases due to dominant propagation directions for the considered period bands.

The spread of group velocity measurements shown in Fig. 7(b) decreases with increasing interstation distance. Beside the fact that there are less accepted measurements, this observation can also be explained either by more path averaging of small-scale medium inhomogeneities or by smaller measurement uncertainty at longer distances as discussed by Gerstoft *et al.* (2006). Indeed, we observe such a trend at 7 and 12 s period in the standard deviations estimated for each individual station pair using the 3-month NCF stacks (grey curves in Fig. 7b). However, the range of uncertainties is

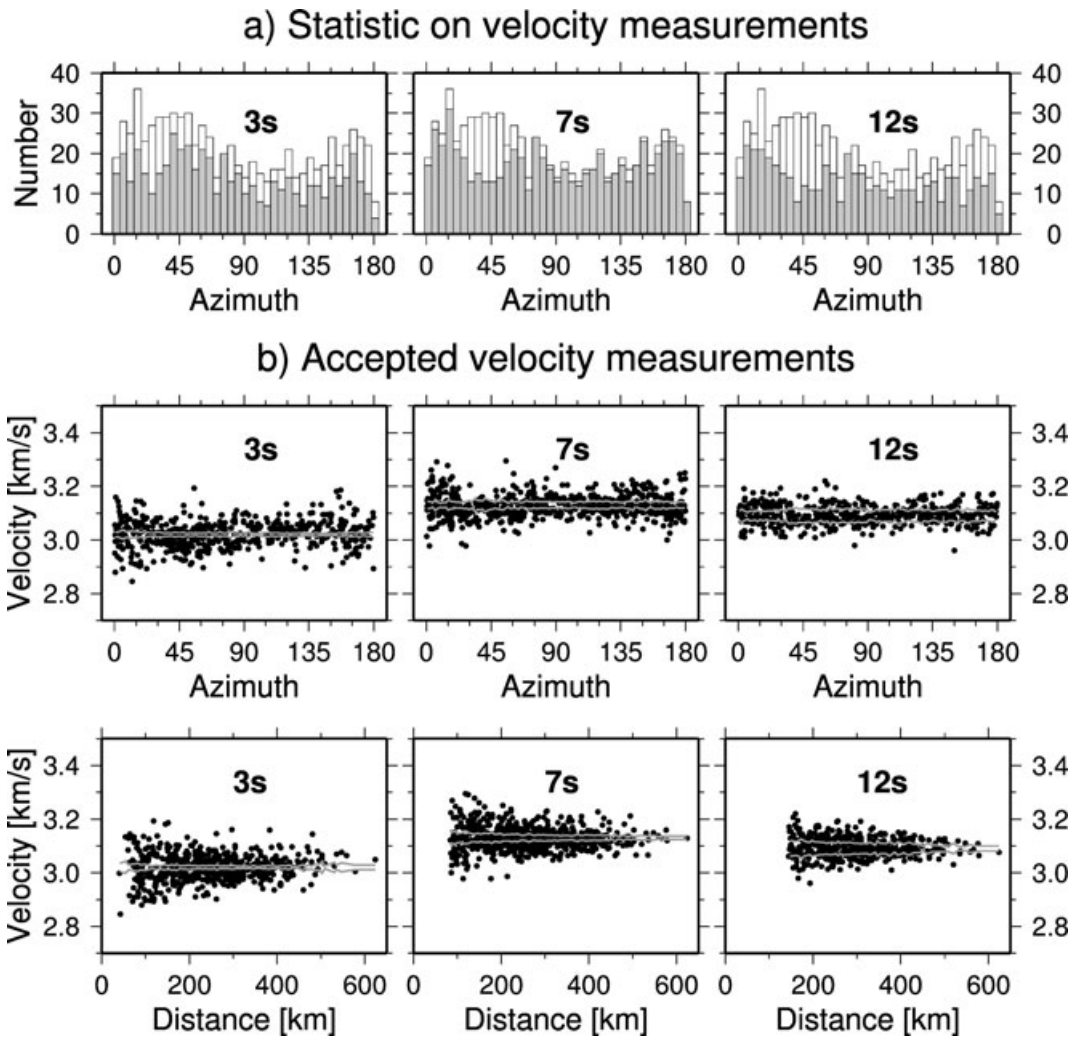

Figure 7. (a) Azimuthal distribution of available station pairs (white bars) and accepted group velocity measurements (grey bars) for three period bands. (b) Accepted group velocity measurements for three period bands and dependency on azimuth (top panels) and interstation distance (bottom panels). For comparison, grey lines visualize standard deviations of individual group velocity measurements obtained from 3-month cross-correlation stacks. Individual velocity standard deviations of station pairs are averaged in 65 km (bottom panels) and 18 degree bins (top panels). Averaged standard deviations are plotted with respect to a mean group velocity obtained from all plotted station pairs: 3.02 km s^{-1} (3 s), 3.13 km s^{-1} (7 s) and 3.09 km s^{-1} (12 s).

clearly smaller than the observed spread of group velocities, which is therefore most likely reflecting inhomogeneities in the studied area.

3 GROUP VELOCITY TOMOGRAPHY

3.1 Results

We perform inversions for Rayleigh wave group velocity maps following the method of Barmin *et al.* (2001). First, we invert for periods of 3, 7 and 12 s (Fig. 8). These period bands sample the range where we obtain a high number of group velocity measurements for most station pairs. We weight each station pair equally during the inversion process. A 0.2 × 0.2 degree grid and a (constant) starting model corresponding to the averaged observed velocity at each period is employed. Different regularization configurations are tested to find the optimal combination of parameters. Finally, we use a weight of $\alpha = 400$ and a correlation length of $\sigma = 40$ km for the Gaussian smoothing function (for details see Barmin *et al.* 2001). We obtain rms reductions between 30 and 40 per cent (Table 1). The final group velocity maps show clear velocity anomalies in the studied area. Lower velocities are yielded for period bands between 3 and 12 s within the Oslo Graben. Higher group velocities are observed for the surrounding areas, in particular northwest of the Oslo Graben. The West of the studied area seems to be characterized by low-velocity anomalies. In Fig. 9, we show the distribution of paths and a resolution estimate based on the method by Barmin *et al.* (2001) for each group velocity map. The resolution shows values below 20 km for the central part of the studied area. Closer to the margins, resolution decreases (values increase to about 35 km), but is still good enough to ensure the reliability of the inverted velocity patterns presented in Fig. 8. We also test different thresholds (conservative and tolerant) for the data selection criteria stated in Section 2 and find no significant differences in the inverted group velocity maps. Furthermore, keeping only one station of the NORSAR array to ensure a more uniform path distribution, does not change the results significantly.

For a further test of the robustness of our results, we invert data from a synthetic velocity model (Fig. 10). Disjoint checkerboard-like input models are used which are characterized by a constant

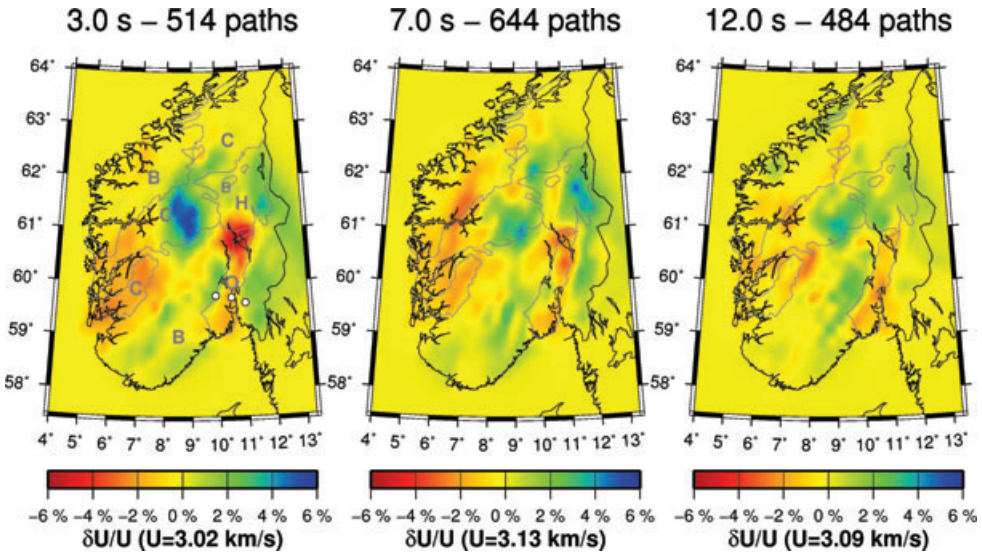

Figure 8. Rayleigh wave group velocity maps inverted from noise cross-correlation functions at 3, 7 and 12 s period. Grey lines indicate main geological units in southern Norway. O: Oslo Graben, B: Precambrian Basement, C: Caledonian nappes, H: Hedmark Group. White-filled circles indicate locations where results are compared with the MAGNUS-REX experiment (Stratford *et al.* 2009).

Table 1. Initial and final rms velocities for Rayleigh wave group velocity tomography.

Periods	3 s	7 s	12 s	25 s
Initial rms	0.0506 km s^{-1}	0.0434 km s^{-1}	0.0367 km s^{-1}	0.0648 km s^{-1}
Final rms	0.0295 km s^{-1}	0.0281 km s^{-1}	0.0265 km s^{-1}	0.0530 km s^{-1}
rms reduction	41.7 per cent	35.3 per cent	27.8 per cent	18.2 per cent

±3 per cent velocity perturbations with respect to the background velocity of 3 km s^{-1} in discrete areas. We compute velocities for all station pairs which are available for the corresponding period by tracing rays through the model. For a second tomography run, Gaussian noise, with a standard deviation σ_{vel} corresponding to the averaged observed measurement error for the respective period, is added to the group velocity computed for each interstation path (3 s: $\sigma_{vel} = 0.007$ km s^{-1}, 7 s: $\sigma_{vel} = 0.013$ km s^{-1}, 12 s: $\sigma_{vel} = 0.022$ km s^{-1}). Without noise, the model is well reconstructed within the central part of the studied area. However, there are smearing effects between velocity anomalies oriented southwest to northeast, which are more pronounced for the inversion of noisy input data. Furthermore, amplitudes of the reconstructed anomalies are slightly underestimated in the west and north. However, the position of the anomalies is still recovered. The reconstruction test shows that the shape and orientation of the small-scale anomalies found in the south (Fig. 8) might be biased by or be artefacts of the inversion.

We also invert a group velocity map at 25 s (Fig. 11). Even if we are more tolerant in the selection criteria (SNR limit: 11; standard deviation limit: 0.1 km s^{-1}; stack number limit: 2), the number of accepted velocity measurements is quite low. Therefore, we use a stronger damping to suppress inversion artefacts and obtain a rather low variance reduction (Table 1). The checkerboard test shows clear smearing effects. Nevertheless, the large-scale trend towards lower velocities in central and northeastern Norway can be interpreted as a robust pattern.

3.2 Discussion

There are no deep and young sedimentary basins in southern Norway which would produce pronounced low-velocity anomalies. Therefore, small variations of about ±3 per cent as inverted from the group velocity measurements between 3 and 12 s period for wide parts of the studied region are not unexpected. The shapes of the anomalies are consistent with the main geological units in southern Norway (see contours in Fig. 8).

Recently, Olesen *et al.* (2010) compiled data from petrophysical sampling programs in Norway including density measurements on bedrock samples. A number of about 28 000 rock samples, collected during geological mapping and geophysical studies, have been used to produce a density map for Norway by calculating the average values within each geological unit. The group velocity anomalies found by our study correlate well with that map. For all inverted period bands, the Oslo Graben is clearly associated with low Rayleigh wave velocities. This result can be explained by relatively low densities of the associated rocks found by Olesen *et al.* (2010) in that area (2600–2700 kg m^{-3}). To the west and east of the Oslo Graben, the Precambrian basement shows expected higher seismic velocities (densities: 2700–2900 kg m^{-3}). The Caledonian nappes in the central part of southern Norway were formed during the Caledonian orogenesis and are oriented southwest to northeast. Within the nappes, we find mostly metamorphic rocks including mafic high-density rocks (2900–3000 kg m^{-3}) which explain the highest velocities found in the area. Furthermore, high velocities are also observed for the Hedmark group to the north of the Oslo Graben. As already mentioned, the velocity patterns to the southwest or west of the Oslo Graben at 3 and 7 s might be biased by lack of resolution. However, for the area of comparable low velocities around 8° E and 60° N, also lower densities (2650–2700 kg m^{-3}) have been reported by Olesen *et al.* (2010) with respect to the surrounding rocks. For the remaining anomalies, it remains uncertain whether they show actual inhomogeneities in the basement rocks.

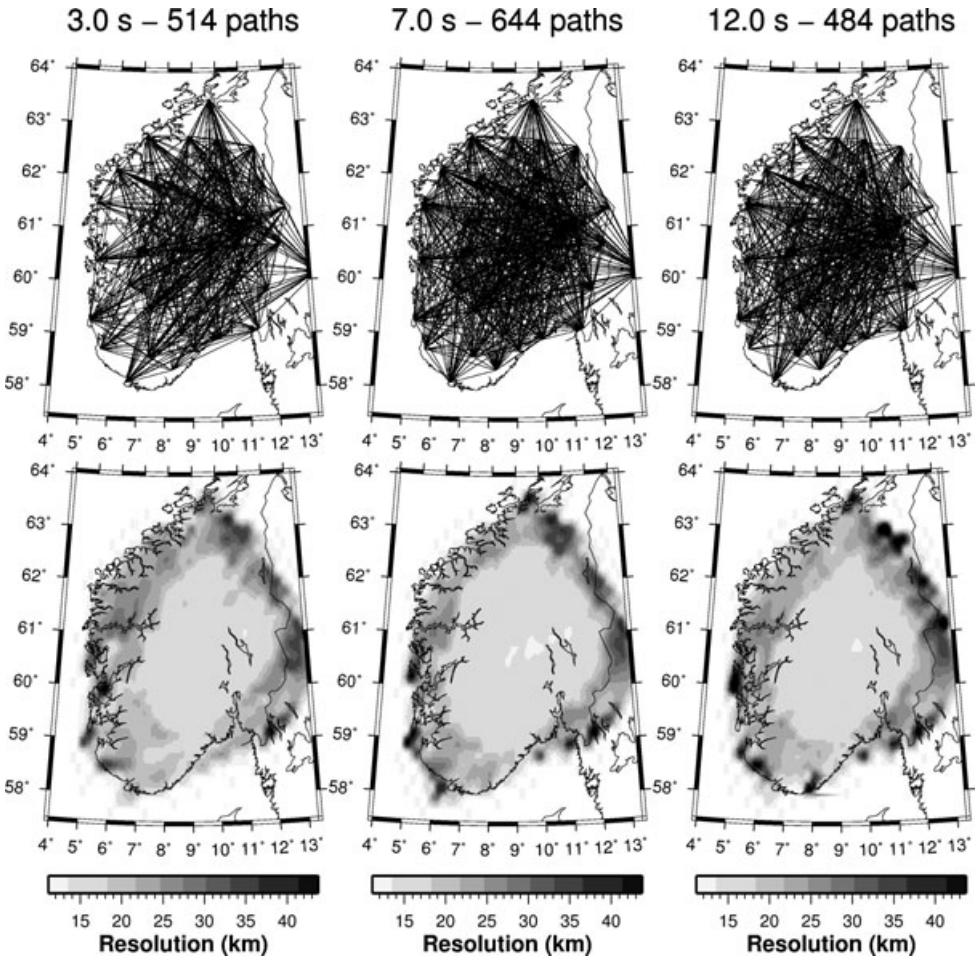

Figure 9. Data coverage and resolution of tomography results shown in Fig. 8 for three different period bands. Upper panels show accepted interstation paths. Lower panels present a resolution estimate.

It is very striking that low velocities are found in the West of the studied area for the shorter period bands. Particularly in the area where we have the Caledonian nappes, we may expect to observe high velocities as found further to the northeast within the same geological unit. This area is characterized by a very rough topography (see Fig. 1). Mountain peaks at 2000 m elevation are cut by deep fjords, which can reach 1000 m depth. Although low velocities can be partially explained by low densities found by Olesen *et al.* (2010), we have also to account for a possible effect of the topography on propagation of the seismic waves. Strong topographic contrasts are expected to lead to an underestimation of velocities which may not be negligible for the considered wavelengths (about 10 km at 3 s period). Impact of topography and scattering on propagation of surface waves has been studied for period bands longer than 10 s by Snieder (1986). To get a first, approximate estimate of the maximum effect of topography on waves at period bands considered here, we compute the difference between measured wave speeds along a flat path and along the surface including the relief between two stations. Although the real effect is probably lower at the given wavelengths, we find that velocities might be underestimated by up to 0.1 km s^{-1} (about 3 per cent) for interstation paths crossing fjords and high mountains (e.g. NWG04-NWG14). Therefore, it might become necessary to correct the group velocity maps before proceeding with a depth inversion for 3-D seismic wave velocity models. The quantification of these errors for each station pair is part of an ongoing study.

We find similar trends for seismic velocities at 3, 7 and 12 s period compared with the upper-crustal *P*-wave velocities published by Stratford *et al.* (2009). In particular, the decrease of wave speeds within the Oslo Graben was also found on both profiles crossing the rift (see Fig. 1). Furthermore, slightly increasing *P*-wave velocities were found in the central part of the studied area at the margin of the Caledonides, where we observe the highest Rayleigh wave velocities. For a quantitative comparison, we compute Rayleigh wave group velocities at 3 s period using the model obtained from the seismic refraction experiment (Stratford *et al.* 2009, 2010) at three locations crossing the Oslo Graben (see Figs 1 and 8). In agreement with the seismic noise tomography, we obtain that Rayleigh wave velocities are about 3 per cent faster outside the graben than inside, although the absolute forward computed velocities are slightly higher along the profile.

At 25 s period the group velocity map looks completely different compared to shorter period bands. We observe higher velocities within the Oslo Graben and close to the Norwegian coastline than in central and northeastern Norway. Even though a group velocity map presents a depth-averaged result, this pattern correlates very well with the variation of Moho depths beneath southern Norway as published by Stratford *et al.* (2009). In particular, a shallower fast

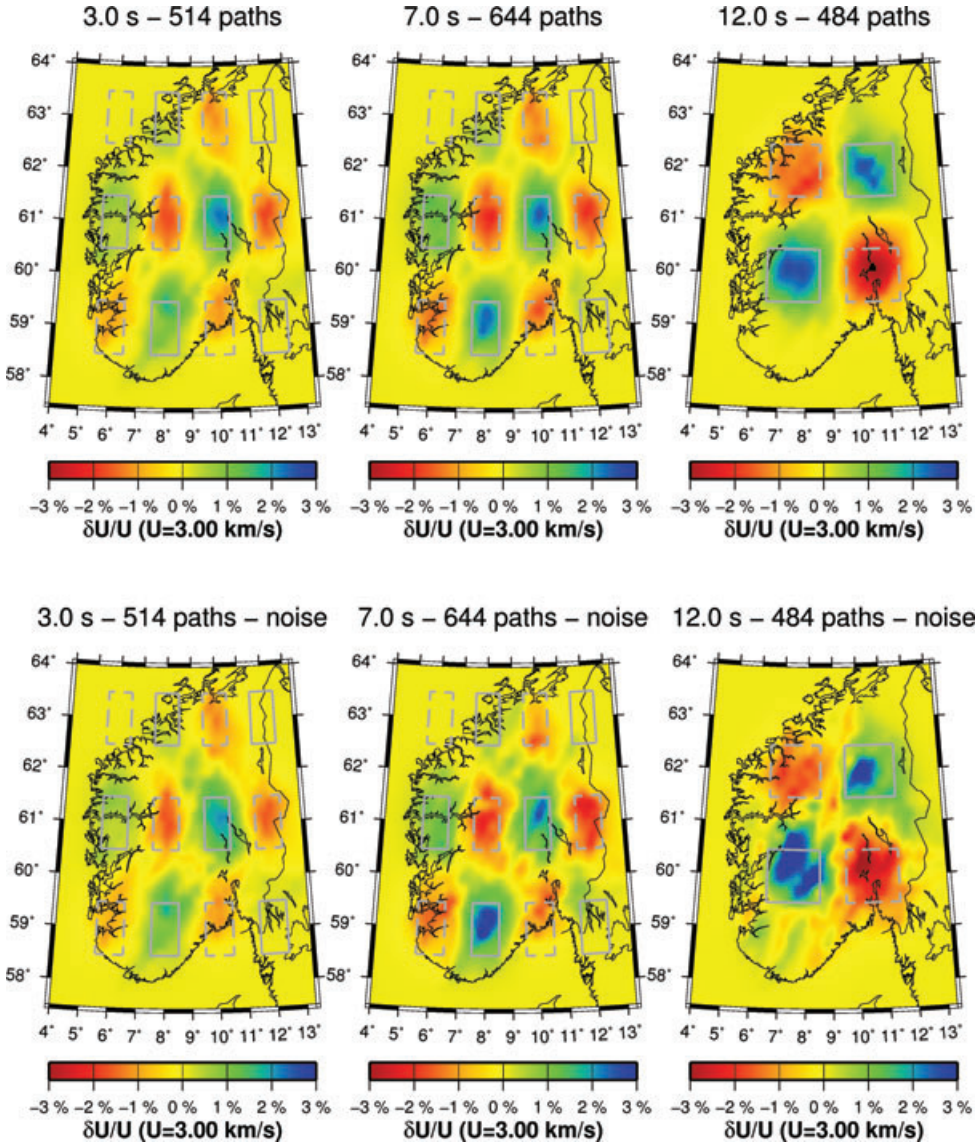

Figure 10. Rayleigh wave group velocity maps inverted from synthetic data at 3, 7 and 12 s period. Grey lines show synthetic velocity model used to compute group velocities for each station pair which is used in the tomography of measured data (see Figs 8 and 9). Dashed and continuous lines indicate discrete areas with (constant) negative and positive velocity perturbation of 3 per cent. Background velocity is 3.0 km s^{-1}. Lower panels show results after adding Gaussian noise to the group velocities computed from the synthetic input model for each interstation path (3 s: $\sigma_{\mathrm{vel}} = 0.007\,\mathrm{km\,s^{-1}}$, 7 s: $\sigma_{\mathrm{vel}} = 0.013\,\mathrm{km\,s^{-1}}$, 12 s: $\sigma_{\mathrm{vel}} = 0.022\,\mathrm{km\,s^{-1}}$).

lithospheric mantle is an expected feature associated with the Oslo Graben.

4 CONCLUSIONS

Within this study, we have computed NCFs from a seismic broadband network in southern Norway. By evaluating SNRs and using f–k analysis, we found that seismic noise is dominantly generated at the close Norwegian coastlines during winter over a wide period range. In summer the noise wavefield appeared to be more diffuse at period bands between 7 and 12 s, which corresponds to secondary and short-period primary ocean microseisms. We found that primary microseisms at longer periods are generated in different, most likely more distant areas during summer. The spatial and temporal distribution of noise sources was found to be sufficiently good to obtain unbiased and reliable Rayleigh wave group velocities from the cross-correlation functions over all azimuths. Tomographic inversion of station pair group velocity data produced group velocity maps at 3, 7 and 12 s period. We found clear velocity anomalies in the studied area, well correlated with upper-crustal inhomogeneities like the Oslo Graben and the Caledonian nappes. Furthermore, clear correlations between velocities and surface rock densities have been observed. Lower velocities (about 3–5 per cent) have been found within the Oslo Graben, whereas the highest velocities (up to 5 per cent) could be assigned to the Caledonian nappes. Surface topography might have a non-negligible effect on measured velocities at the given wavelengths and might contribute to the low-velocity anomalies in the West of southern Norway. This potentially existing bias has to be removed before 3-D models of the region can be produced. We have also used a low number of group velocity measurements at

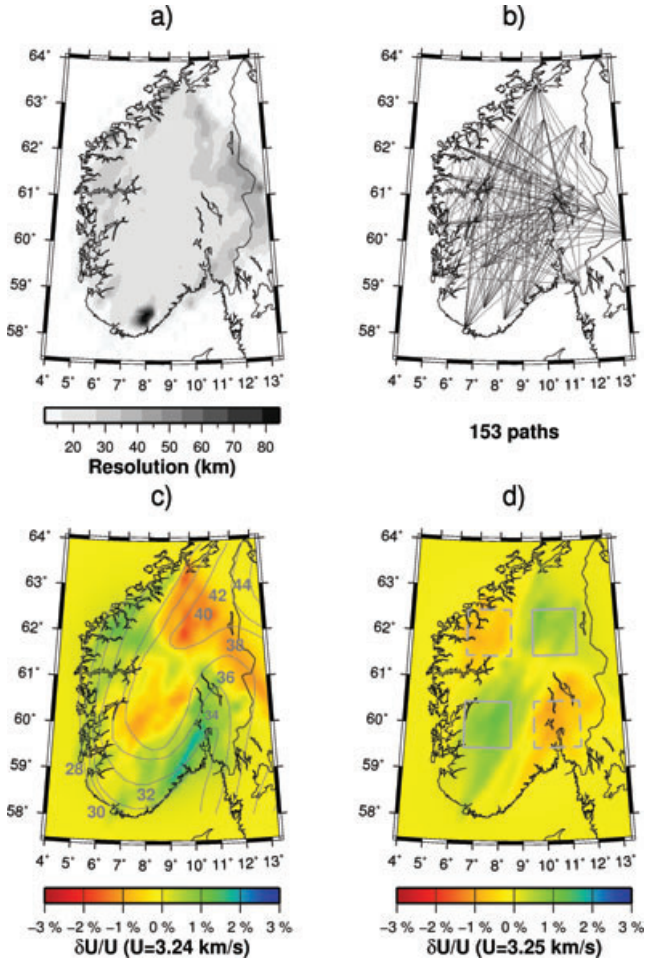

Figure 11. Rayleigh wave group velocity tomography at 25 s period. (a) Resolution of tomography. (b) Data coverage. (c) Group velocity map inverted from noise cross-correlation functions. Grey lines indicate Moho depth contours in kilometres from Stratford *et al.* (2009). (d) Inversion of synthetic data as explained in Fig. 10 (no Gaussian noise, background velocity is 3.25 km s^{-1}).

25 s period to get a group velocity map at this period. A large-scale pattern could be observed which is different from the upper-crustal anomalies and which correlates well with the variation of Moho depth in southern Norway.

ACKNOWLEDGMENTS

MAGNUS waveforms were recorded with the mobile KArlsruhe Broadband Array of the Karlsruhe Institute of Technology (KIT), Germany as well as with permanent stations of the NORSAR array, the Norwegian National Seismological Network and GSN. Continuous data from the NORSAR array were kindly provided by Johannes Schweitzer. Financial support for the MAGNUS experiment was provided by the Universities of Aarhus, Copenhagen, Karlsruhe and Oslo as well as NORSAR. This work has been done in the framework of the ESF EUROCORES TOPO-EUROPE Program 07-TOPO-EUROPE-FP-014. We acknowledge financial support from the Research Council of Norway. We appreciate the comments and suggestions of both anonymous reviewers which helped to improve this manuscript. Figures have been prepared using the Generic Mapping tools (Wessel & Smith 1998).

REFERENCES

Aki, K., 1957. Space and time spectra of stationary stochastic waves, with special reference to microtremors, *Bull. Earthquake Res. Inst. Tokyo Univ.,* **35,** 415–457.

Barmin, M., Ritzwoller, M. & Levshin, A., 2001. A fast and reliable method for surface wave tomography, *Pure appl. Geophys.,* **158**(8), 1351–1375.

Bensen, G., Ritzwoller, M., Barmin, M., Levshin, A., Lin, F., Moschetti, M., Shapiro, N. & Yang, Y., 2007. Processing seismic ambient noise data to obtain reliable broad-band surface wave dispersion measurements, *Geophys. J. Int.,* **169**(3), 1239–1260.

Duvall, T., Jeffferies, S., Harvey, J. & Pomerantz, M., 1993. Time-distance helioseismology, *Nature,* **362,** 430–432.

Essen, H., Krüger, F., Dahm, T. & Grevemeyer, I., 2003. On the generation of secondary microseisms observed in northern and central Europe, *J. geophys. Res.,* **108**(B10), 2506, doi:10.1029/2002JB002338.

Friedrich, A., Krüger, F. & Klinge, K., 1998. Ocean-generated microseismic noise located with the Gräfenberg array, *J. Seismol.,* **2**(1), 47–64.

Gerstoft, P., Sabra, K., Roux, P., Kuperman, W. & Fehler, M., 2006. Green's functions extraction and surface-wave tomography from microseisms in southern California, *Geophysics,* **71**(4), SI23–SI31.

Gouédard, P. *et al.*, 2008. Cross-correlation of random fields: mathematical approach and applications, *Geophys. Prospect.,* **56**(3), 375–394.

Gutenberg, B., 1936. On microseisms, *Bull. seism. Soc. Am.,* **26**(2), 111–117.

Havskov, J. & Ottemöller, L., 1999. Electronic Seismologist - SeisAn Earthquake analysis software, *Seism. Res. Lett.,* **70,** 532–534.

Larose, E. *et al.*, 2006. Correlation of random wavefields: an interdisciplinary review, *Geophysics,* **71**(4), SI11–SI21.

Larose, E., Roux, P. & Campillo, M., 2007. Reconstruction of Rayleigh-Lamb dispersion spectrum based on noise obtained from an air-jet forcing, *J. acoust. Soc. Am.,* **122**(6), 3437–3444.

Levshin, A., Yanovskaya, T., Lander, A., Bukchin, B., Barmin, M., Ratnikova, L. & Its, E., 1989. *Seismic Surface Waves in a Laterally Inhomogeneous Earth*, ed. Keilis-Borok, V.I., Kluwer, Norwell, MA.

Lin, F., Ritzwoller, M., Townend, J., Bannister, S. & Savage, M., 2007. Ambient noise Rayleigh wave tomography of New Zealand, *Geophys. J. Int.,* **170**(2), 649–666.

Lin, F., Moschetti, M. & Ritzwoller, M., 2008. Surface wave tomography of the western United States from ambient seismic noise: Rayleigh and Love wave phase velocity maps, *Geophys. J. Int.,* **173**(1), 281–298.

Longuet-Higgins, M., 1950. A theory of the origin of microseisms, *Philosophical Transactions of the Royal Society of London. Series A. Mathematical and Physical Sciences,* **243**(857), 1–35.

Moschetti, M., Ritzwoller, M. & Shapiro, N., 2007. Surface wave tomography of the western United States from ambient seismic noise: Rayleigh wave group velocity maps, *Geochem. Geophys. Geosyst.,* **8**(8), Q08010, doi:10.1029/2007GC001655.

Ohrnberger, M., 2001. Continuous automatic classification of seismic signals of volcanic origin at Mt. Merapi, Java, Indonesia, *PhD thesis,* University of Potsdam, http://opus.kobv.de/ubp/volltexte/2005/31/pdf/ohrnberg.pdf [last accessed 2010 July 05].

Olesen, O. *et al.*, 2010. New aeromagnetic and gravity compilations from Norway and adjacent areas: methods and applications, in *Petroleum Geology: From Mature Basins to New Frontiers. Proceedings of the 7th Petroleum Geology Conference.*, pp. 559–586, eds, Vining, B.A. & Pickering, S.L., Geological Society of London.

Pedersen, H., Krüger, F. & the SVEKALAPKO Seismic Tomography Working Group, 2007. Influence of the seismic noise characteristics on noise correlations in the Baltic shield, *Geophys. J. Int.,* **168**(1), 197–210.

Ritzwoller, M. & Levshin, A., 1998. Eurasian surface wave tomography: group velocities, *J. geophys. Res.,* **103,** 4839–4878.

Roux, P. & Kuperman, W., 2004. Extracting coherent wave fronts from acoustic ambient noise in the ocean, *J. acoust. Soc. Am.,* **116**(4), 1995–2003.

Roux, P., Sabra, K., Kuperman, W. & Roux, A., 2005. Ambient noise cross correlation in free space: theoretical approach, *J. acoust. Soc. Am.,* **117**(1), 79–84.

Sabra, K., Gerstoft, P., Roux, P., Kuperman, W. & Fehler, M., 2005a. Extracting time-domain Green's function estimates from ambient seismic noise, *Geophys. Res. Lett.,* **32,** L03310, doi:10.1029/2004GL021862.

Sabra, K., Gerstoft, P., Roux, P., Kuperman, W. & Fehler, M., 2005b. Surface wave tomography from microseisms in Southern California, *Geophys. Res. Lett.,* **32,** L14311.

Shapiro, N. & Campillo, M., 2004. Emergence of broadband Rayleigh waves from correlations of the ambient seismic noise, *Geophys. Res. Lett.,* **31**(7), 1615–1619.

Shapiro, N., Campillo, M., Stehly, L. & Ritzwoller, M., 2005. High-resolution surface-wave tomography from ambient seismic noise, *Science,* **307**(5715), 1615–1618.

Snieder, R., 1986. The influence of topography on the propagation and scattering of surface waves, *Phys. Earth planet. Int.,* **44,** 226–241.

Snieder, R., 2004. Extracting the Green's function from the correlation of coda waves: a derivation based on stationary phase, *Phys. Rev. E,* **69**(4), 46610, doi:10.1103/PhysRevE.69046610.

Stehly, L., Campillo, M. & Shapiro, N., 2006. A study of the seismic noise from its long-range correlation properties, *J. geophys. Res.,* **111,** B10306, doi:10.1029/2005JB004237.

Stehly, L., Campillo, M., Froment, B. & Weaver, R., 2008. Reconstructing Green's function by correlation of the coda of the correlation (C3) of ambient seismic noise, *J. geophys. Res.,* **113,** B11306, doi:10.1029/2008JB005693.

Stehly, L., Fry, B., Campillo, M., Shapiro, N., Guilbert, J., Boschi, L. & Giardini, D., 2009. Tomography of the Alpine region from observations of seismic ambient noise, *Geophys. J. Int.,* **178**(1), 338–350.

Stratford, W., Thybo, H., Faleide, J., Olesen, O. & Tryggvason, A., 2009. New Moho Map for onshore southern Norway, *Geophys. J. Int.,* **178**(3), 1755–1765.

Stratford, W., Thybo, H. & Frassetto, A., 2010. Moho depth and age in southern Norway, *European Geosciences Union General Assembly, Vienna, Mai 2010, Geophysical Research Abstracts,* **12** (abst. 07508).

Tsai, V., 2009. On establishing the accuracy of noise tomography travel-time measurements in a realistic medium, *Geophys. J. Int.,* **178**(3), 1555–1564.

Weaver, R., Froment, B. & Campillo, M., 2009. On the correlation of non-isotropically distributed ballistic scalar diffuse waves., *J. acoust. Soc. Am.,* **126**(4), 1817–1826.

Weidle, C. & Maupin, V., 2008. An upper-mantle*S*-wave velocity model for Northern Europe from Love and Rayleigh group velocities, *Geophys. J. Int.,* **175**(3), 1154–1168.

Weidle, C. *et al.*, 2010. MAGNUS: a seismological broadband experiment to resolve crustal and upper mantle structure beneath the southern Scandes mountains in Norway, *Seismol. Res. Lett.,* **81**(1), 76–84.

Wessel, P. & Smith, W., 1998. New improved version of GMT released, *EOS, Trans. Am. geophys. Un.,* **79,** 579.

Yang, Y., Ritzwoller, M., Levshin, A. & Shapiro, N., 2006. Ambient noise Rayleigh wave tomography across Europe, *Geophys. J. Int.,* **168**(1), 259–274.

Yao, H. & van der Hilst, R., 2009. Analysis of ambient noise energy distribution and phase velocity bias in ambient noise tomography, with application to SE Tibet, *Geophys. J. Int.,* **179**(2), 1113–1132.

Yao, H., van der Hilst, R. & de Hoop, M., 2006. Surface-wave array tomography in SE Tibet from ambient seismic noise and two-station analysis-I. Phase velocity maps, *Geophys. J. Int.,* **166**(2), 732–744.

Yao, H., Beghein, C. & van der Hilst, R., 2008. Surface wave array tomography in SE Tibet from ambient seismic noise and two-station analysis-II. Crustal and upper-mantle structure, *Geophys. J. Int.,* **173**(1), 205–219.